

Osmium Complexes with Tridentate 6-Pyrazol-3-yl 2,2'-Bipyridine Ligands: Coarse Tuning of Phosphorescence from the Red to the Near-Infrared Region

Kellen Chen,^[a] Yi-Ming Cheng,^[a] Yun Chi,^{*,[a]} Mei-Lin Ho,^[b] Chin-Hung Lai,^[b] Pi-Tai Chou,^{*,[b]} Shie-Ming Peng,^[b] and Gene-Hsiang Lee^[b]

Abstract: We have prepared and characterized a series of osmium complexes [Os₂(CO)₄(fpbpy)₂] (**1**), [Os(CO)(fpbpy)₂] (**2**), and [Os(fpbpy)₂] (**3**) with tridentate 6-pyrazol-3-yl 2,2'-bipyridine chelating ligands. Upon the transformation of complex **2** into **3** through the elimination of the CO ligand, an extremely large change in the phosphorescence wavelength from 655 to 935 nm was observed. The results are rationalized qualitatively by the strong π -accepting character of CO, which lowers the energy of the osmium d _{π} orbital, in combination with the lower degree of π conjugation in **2** owing to

the absence of one possible pyridine-binding site. As a result, the energy gap for both intraligand π - π^* charge transfer (ILCT) and metal-to-ligand charge transfer (MLCT) is significantly greater in **2**. Firm support for this explanation was also provided by the time-dependent DFT approach, the results of which led to the conclusion that the S₀→T₁ transition mainly involves MLCT between the osmium

center and bipyridine in combination with pyrazolate-to-bipyridine $^3\pi$ - π^* ILCT. The relatively weak near-infrared emission can be rationalized tentatively by the energy-gap law, according to which the radiationless deactivation may be governed by certain low-frequency motions with a high density of states. The information provided should allow the successful design of other emissive tridentate metal complexes, the physical properties of which could be significantly different from those of complexes with only a bidentate chromophore.

Keywords: N ligands • near-infrared region • osmium • phosphorescence • pi interactions

Introduction

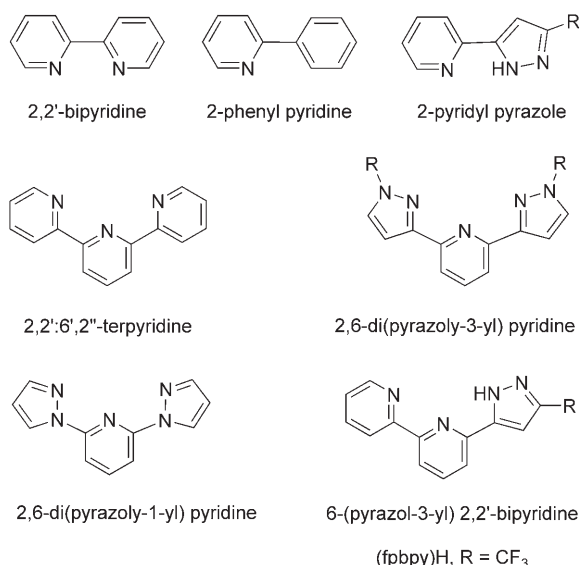
Transition-metal complexes that incorporate simple bidentate diimine ligands such as 2,2'-bipyridine (bpy),^[1] cyclometalated ligands such as 2-phenylpyridine (ppy),^[2] or C-linked ligands such as 2-pyridylpyrazole^[3] have attracted a great deal of interest in recent years. Research focused on this area has been motivated principally by the use of these complexes in the study of excited-state electron- and

energy-transfer processes^[4] as well as potential applications in the fabrication of chemical sensors, photovoltaics, and organic light-emitting diodes (OLEDs).^[5] In sharp contrast to 2,2'-bipyridine, the 2-phenylpyridine ligand can react with transition-metal reagents through direct C-H bond activation to give the cyclometalated products.^[6] Similarly, as a result of the high acidity of the pyrazole N-H bond, C-linked 2-pyridylpyrazole is expected to be even more reactive and could be used to extend the scope of the cyclometalation reaction, particularly to third-row transition-metal reagents, which are known to be less reactive than their first- and second-row counterparts. Moreover, the strong σ -donor property of the pyrazolate unit, together with the good π -accepting ability of the second pyridyl fragment,^[7] may provide a synergism of electron delocalization over the whole π -conjugated system of the ligand and the metal d _{π} orbitals.

Parallel to the chemistry of bidentate chelates, tridentate ligands such as 2,2':6',2''-terpyridine (tpy) and its functionalized derivatives have also been the subject of extensive investigations.^[8] The popularity of terpyridine ligands is easily

[a] K. Chen, Dr. Y.-M. Cheng, Prof. Y. Chi
Department of Chemistry
National Tsing Hua University
Hsinchu 300 (Taiwan)
Fax: (+886) 3-572-0864
E-mail: ychi@mx.nthu.edu.tw

[b] M.-L. Ho, C.-H. Lai, Prof. P.-T. Chou, Prof. S.-M. Peng, G.-H. Lee
Department of Chemistry and Instrumentation Center
National Taiwan University
Taipei 106 (Taiwan)
Fax: (+886) 2-2369-5208
E-mail: chop@ntu.edu.tw



understood. On the one hand, they can bind to a variety of metal ions in various low and high oxidation states to give complexes with novel redox chemistry and luminescent properties. On the other hand, their tailor-made molecular environments for chelating interactions would give much necessary stabilization and special physical properties to the resulting metal complexes. Recently, these investigations have been extended to other tridentate systems based on 2,6-dipyrazolylpyridine and its derivatives, namely, 2,6-dipyrazol-1-yl and 2,6-dipyrazol-3-ylpyridine.^[9] As the functionalized heterocycles in these tridentate ligands have distinct basicities and π -orbital energies associated with them, the intrinsic chemical and physical characteristics of the resulting metal complexes should be altered notably. The apparently similar ligand 6-pyrazol-3-yl-2,2'-bipyridine was also designed and synthesized, with the expectation that the terminal C-linked pyrazole fragment may undergo a deprotonation reaction to form the distinctive anionic chelate,^[10] or react with KBH₄ to give a pyrazoyl borate ligand with two tridentate chelating arms linked by a BH₂ spacer.^[11] The chemistry of this borate ligand contrasts sharply with the conventional chemistry of neutral terpyridine-type ligands.

Abstract in Chinese:

我們在此報告一系列含鉍合性、三芽取代基 6-(pyrazol-3-yl) 2,2'-bipyridine 鐵金屬錯合物 1-3 的合成，並藉由基礎理論計算瞭解它們的磷光放射信號由深紅部位 655 nm (2) 位移至近紅外光區 (935 nm, 3) 的調光現象。對於單鐵錯合物 2 而言，由於它的 CO 官能基具有牽引 π 電子的性質，故可降低鐵中心金屬 d_{π} 能階，同時也由於吡啶與鐵金屬間共軌的部分破壞，所以錯合物 2 的 ILCT 與 MLCT 激態能階會較為升高。此外，錯合物 3 的放光出現在近紅外光區，放光量子產率降低，是受到低頻高密度震動態的影響，符合能差定律的預測。最後，本文所獲的各項資訊，將有助於繼續開發其它含有類似三芽取代基之錯合物，預期物理性質將與傳統的雙芽螯合物全然不同。

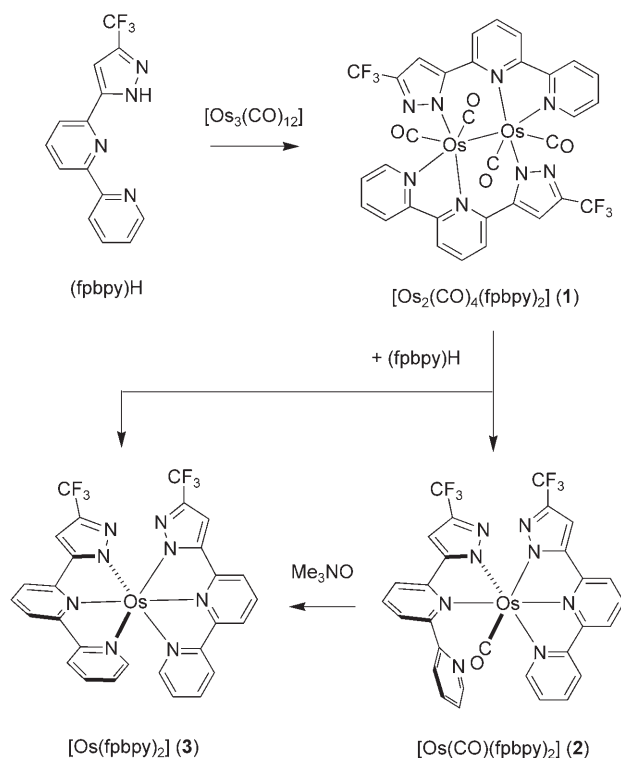
We have made great efforts towards our aim to exploit such tridentate ligands for the construction of promising luminescent molecules. Herein, we describe the reaction of the tridentate ligand 6-(5-(trifluoromethyl)pyrazol-3-yl)-2,2'-bipyridine, denoted as (fpbpy)H, with the osmium carbonyl reagent [Os₃(CO)₁₂], and the chemistry and photophysical properties of the corresponding complexes. The CF₃ substituent introduced at the pyrazolate C5 position not only increases the N-H acidity of the pyrazole owing to the increased electron-withdrawing effect, but also minimizes the number of possible products by blocking the adjacent nitrogen atom, to which the incoming bulky electrophilic reagents are inaccessible. All reaction intermediates en route to the final octahedral complex [Os(fpbpy)₂] were isolated and characterized, so that the mechanism of the assembly process between the metal and the ligands could be deduced. Moreover, comparative photophysical studies of these complexes were carried out along with theoretical studies to gain detailed insight into the excited-state behavior of these complexes. Ultimately, we hope that information of this sort will allow the successful strategic design of other emissive tridentate metal complexes, the physical properties of which could be significantly different from those of complexes with only bidentate ligands.^[12]

Results and Discussion

Synthesis and Characterization

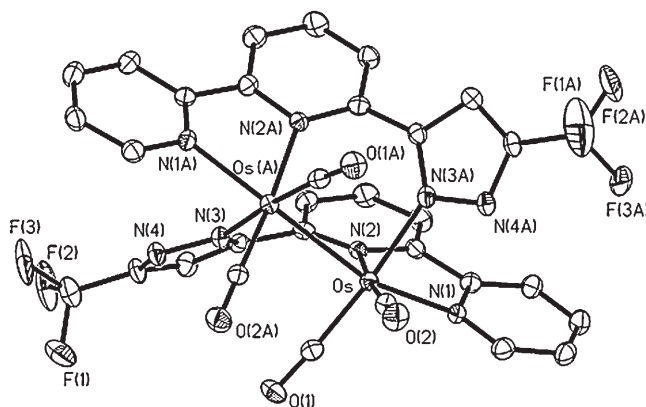
The required tridentate ligand (fpbpy)H was obtained by a Claisen condensation between 6-acetyl-2,2'-bipyridine and ethyl trifluoroacetate, followed by treatment with excess hydrazine hydrate in ethanol at reflux according to established procedures.^[13,14] The subsequent reactions of (fpbpy)H with [Os₃(CO)₁₂] are summarized in Scheme 1. Heating of a 3:1 mixture of (fpbpy)H and the osmium complex [Os₃(CO)₁₂] in diethylene glycol monoethyl ether (DGME; 170 °C, 24 h) led to the formation of the complex [Os₂(CO)₄(fpbpy)₂] (**1**) as an air-stable red crystalline solid. On the other hand, the treatment of [Os₃(CO)₁₂] with 6 equivalents of (fpbpy)H in DGME under similar conditions afforded a bright-red monometallic complex **2** with the formula [Os(CO)(fpbpy)₂] as the major product. Similarly, the treatment of **1** with the decarbonylation reagent Me₃NO, followed by heating in presence of the ligand (fpbpy)H led to the isolation of a mixture of the starting material **1**, monometallic **2**, and [Os(fpbpy)₂] (**3**); the third complex possesses no carbonyl ligand, as indicated by the subsequent spectral analysis. In good agreement with this observation, the treatment of **2** with Me₃NO (180 °C, 12 h) afforded the expected decarbonylation product **3** in 64% yield calculated on the basis of the consumption of **2**, to confirm the status of **2** as a reaction intermediate.

The identities of all complexes were fully established by mass spectrometry, as well as NMR and IR spectroscopy, satisfactory elemental analyses, and structural studies. The IR spectrum of **1** in CH₂Cl₂ solution showed four ν (CO) sig-

Scheme 1. Synthetic routes to osmium complexes **1**–**3**.

nals spanning the region $\tilde{\nu}=2010\text{--}1908\text{ cm}^{-1}$. FAB mass spectrometry of **2** and **3** revealed the respective molecular ion (M^+) signals at m/z 798 and 770 to provide clear evidence for the presence of two fpbpy ligands bonded to the Os^{II} metal center, as well as the incorporation of one CO ligand in the case of **2**. In good agreement with these findings, the IR spectrum of **2** in CH_2Cl_2 showed a single $\nu(\text{CO})$ absorption at $\tilde{\nu}=1973\text{ cm}^{-1}$, whereas the ^1H NMR spectrum of **3** revealed a pattern corresponding to only one set of fpbpy signals as a result of the inherent C_2 symmetry.

A single-crystal X-ray diffraction study was carried out on **1** to reveal its exact molecular structure. As indicated in Figure 1, the structure shows the presence of two osmium atoms separated by a distance $2.7446(4)\text{ \AA}$ on which two chelating pyrazolate ligands reside in mutually *cis* orientations. The terminal pyridyl group occupies the axial position of one osmium atom with the shortest Os–N distance (Os–N(1) = $2.145(4)\text{ \AA}$), whereas the central pyridyl group and the pyrazolate group of the same ligand are located at the equatorial sites of two different osmium atoms with Os–N distances of $2.164(4)\text{ \AA}$ (Os–N(2)) and $2.111(4)\text{ \AA}$ (Os(A)–N(3) \equiv Os–N(3A)), respectively (Tables 1 and 2). This bridging arrangement causes the osmium-bonded fragments to adopt a staggered arrangement, in such a way that the ligands can interact with the central Os–Os unit with a minimum of torsional-strain energy. Finally, there exists a crystallographically imposed C_2 symmetry, for which the C_2 rotational axis is located parallel to both pyrazolate ligands and cuts through the middle of the Os–Os vector.

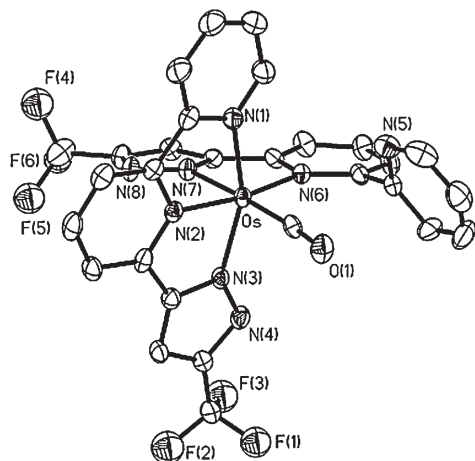
Figure 1. ORTEP diagram of complex **1** with thermal ellipsoids shown at the 30% probability level.Table 1. Crystal data and structure-refinement parameters for complexes **1**, **2**, and **3**.

	1	2	3
Empirical formula	$\text{C}_{40}\text{H}_{40}\text{F}_6\text{N}_8\text{O}_8\text{Os}_2\text{S}_4$	$\text{C}_{29}\text{H}_{16}\text{F}_6\text{N}_8\text{O}_8\text{Os}$	$\text{C}_{31.5}\text{H}_{32}\text{F}_6\text{N}_8\text{O}_{4.5}\text{Os}$
Formula weight	1383.44	796.70	898.85
Temperature	230(2) K	295(2) K	150(2) K
Crystal system	monoclinic	triclinic	monoclinic
Space group	$C2/c$	$P\bar{1}$	$C2/c$
a [\AA]	30.7255(17)	9.8008(5)	32.1185(16)
b [\AA]	9.2968(5)	10.0893(5)	15.4756(7)
c [\AA]	18.2142(10)	15.7952(7)	13.9555(7)
α [$^\circ$]		80.900(1)	
β [$^\circ$]	111.188(1)	86.268(1)	104.220(1)
γ [$^\circ$]		62.750(1)	
V [\AA^3], Z	4851.1(5), 4	1371.0(1), 2	6724.1(6), 8
ρ_{calcd} [g cm^{-3}]	1.894	1.930	1.776
Absorption coefficient [mm^{-1}]	5.486	4.733	3.878
$F(000)$	2680	768	3544
Crystal size [mm^3]	$0.23 \times 0.15 \times 0.15$	$0.10 \times 0.10 \times 0.04$	$0.15 \times 0.15 \times 0.10$
Reflections collected	22 552	18 453	25 580
Independent reflections	5562	6293	7714
$[R(\text{int}) = 0.0437]$		$[R(\text{int}) = 0.0595]$	$[R(\text{int}) = 0.0414]$
Max., min. transmission	0.4933, 0.3651	0.8333, 0.6490	0.6978, 0.5939
Data/restraints/parameters	5562/0/345	6293/0/400	7714/0/461
Goodness-of-fit on F^2	1.123	1.168	1.156
Final R indices ($I > 2\sigma(I)$)	$R_1 = 0.0321$, $wR_2 = 0.0782$	$R_1 = 0.0469$, $wR_2 = 0.0894$	$R_1 = 0.0342$, $wR_2 = 0.0817$
R indices (all data)	$R_1 = 0.0419$, $wR_2 = 0.0898$	$R_1 = 0.0597$, $wR_2 = 0.0934$	$R_1 = 0.0435$, $wR_2 = 0.0941$
Largest diff. peak, hole [e \AA^{-3}]	1.672, -1.095	1.276, -1.233	1.324, -1.264

Complex **2** was also subjected to X-ray structural determination. As shown in Figure 2, its overall coordination geom-

Table 2. Selected bond lengths [\AA] and angles [$^\circ$] for complex **1**.

Os–Os(A)	2.7446(4)	Os–N(1)	2.145(4)
Os–N(2)	2.164(4)	Os–N(3A)	2.111(4)
Os–C(1)	1.852(5)	Os–C(2)	1.850(5)
$\angle \text{N(1)–Os–N(2)}$	75.70(15)	$\angle \text{N(1)–Os–Os(A)}$	162.32(11)
$\angle \text{N(2)–Os–C(2)}$	174.93(18)	$\angle \text{N(3A)–Os–C(1)}$	174.75(18)

Figure 2. ORTEP diagram of complex **2** with thermal ellipsoids shown at the 30% probability level.

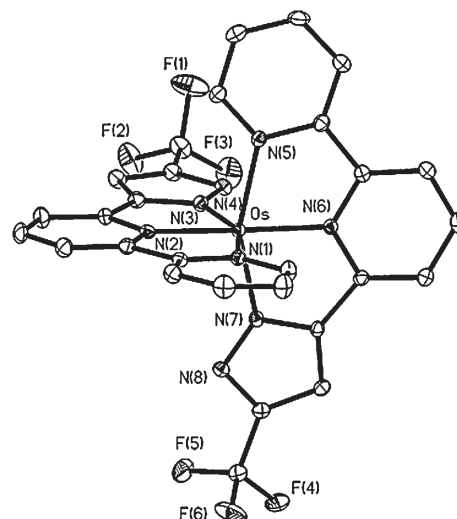
etry is best described as a distorted octahedron. One fpbpy ligand serves as a typical tridentate chelating ligand with a significantly shorter Os–N bond to the middle pyridyl fragment (Os–N(2) = 1.997(5) \AA) than those to the outer chelate rings (Os–N(1) = 2.094(5), Os–N(3) = 2.053(5) \AA). The second fpbpy ligand adopts an unusual bidentate mode of binding with slightly elongated distances (Os–N(6) = 2.150(5), Os–N(7) = 2.085(5) \AA ; Tables 1 and 3). The re-

Table 3. Selected bond lengths [\AA] and angles [$^\circ$] for complex **2**.

Os–N(1)	2.094(5)	Os–N(2)	1.997(5)
Os–N(3)	2.053(5)	Os–N(6)	2.150(5)
Os–N(7)	2.085(5)	Os–C(1)	1.831(7)
$\angle \text{N(1)–Os–N(2)}$	78.5(2)	$\angle \text{N(2)–Os–N(3)}$	78.8(2)
$\angle \text{N(6)–Os–N(7)}$	77.79(18)	$\angle \text{N(7)–Os–C(1)}$	175.2(2)

maining, sixth coordination site of **2** is occupied by a unique π -accepting CO ligand, which is adjacent to the uncoordinated pendant pyridyl group. This observed coordination geometry is akin to that of such complexes as $[\text{Ru}(\text{tpy})(\text{bpy})(\text{H}_2\text{O})]^{2+}$ and $[\text{Os}(\text{tpy})(\text{bpy})(\text{H}_2\text{O})]^{2+}$,^[15] in which tridentate, bidentate, and monodentate ligands coordinate simultaneously to the central metal cation.

Finally, to gain more understanding about the general coordination mode of this type of tridentate ligand, we also investigated the crystal structure of the symmetric species **3** (Figure 3, Tables 1 and 4). The observed structural parameters of **3** are in good agreement with those of the portion of

Figure 3. ORTEP diagram of complex **3** with thermal ellipsoids shown at the 30% probability level.Table 4. Selected bond lengths [\AA] and angles [$^\circ$] for complex **3**.

Os–N(1)	2.051(4)	Os–N(2)	1.984(4)
Os–N(3)	2.055(4)	Os–N(5)	2.049(4)
Os–N(6)	1.986(4)	Os–N(7)	2.052(4)
$\angle \text{N(1)–Os–N(2)}$	78.18(15)	$\angle \text{N(2)–Os–N(3)}$	78.22(15)
$\angle \text{N(1)–Os–N(3)}$	156.41(16)	$\angle \text{N(5)–Os–N(6)}$	78.29(15)
$\angle \text{N(6)–Os–N(7)}$	78.13(15)	$\angle \text{N(5)–Os–N(7)}$	156.29(16)

complex **2** containing the tridentate fpbpy ligand. Apparently, the removal of CO and simultaneous coordination of pyridine impose only minimal structural reorganization in this class of metal complexes. This observation is in sharp contrast to the large differences in the photophysical properties described below for these complexes.

Photophysical Properties

The absorption and luminescence spectra recorded for complexes **1–3** in CH_3CN are depicted in Figure 4. The absorption bands with a high extinction coefficient at approximately 325 nm ($\epsilon = 19\,200\text{ M}^{-1}\text{ cm}^{-1}$) for **1**, 385 nm ($\epsilon = 17\,130\text{ M}^{-1}\text{ cm}^{-1}$) for **2**, and 465 nm ($\epsilon = 9\,900\text{ M}^{-1}\text{ cm}^{-1}$) for **3** were assigned to the spin-allowed $^1\pi\text{--}\pi^*$ transition of the fpbpy ligands. The difference in the wavelength at which the peak for the fpbpy ligand occurs can be rationalized by the distinctly different coordinating environments in **1–3**. Drastic differences in the lower-frequency transitions were also observed among **1–3**: The first transition band ($\epsilon \approx 2000\text{ M}^{-1}\text{ cm}^{-1}$) was located at approximately 515, 525, and as high as 715 nm for complexes **2**, **1**, and **3**, respectively. As supported by the later theoretical approach, the corresponding first transition can be ascribed mainly to the spin-allowed metal-to-bipyridine-ligand transition ($^1\text{MLCT}$) in combination with an intraligand charge-transfer transition from the pyrazolate to the bipyridine moieties ($^1\text{ILCT}$). It is

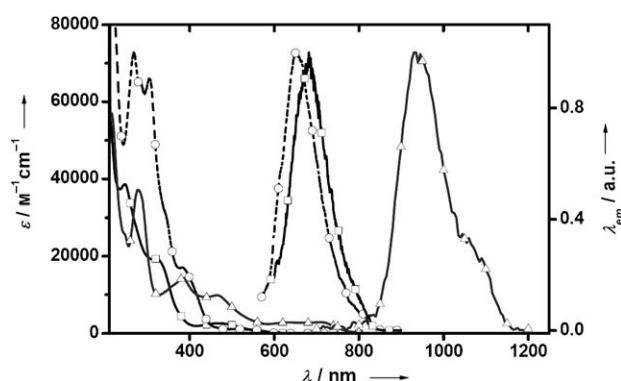


Figure 4. UV/Vis absorption spectra of complexes **1–3** as solutions in acetonitrile at room temperature. Normalized emission spectra of complex **2** (○) in acetonitrile at 298 K and **1** (□) and **3** (△) in acetonitrile at 77 K. The cut-off of the emission spectra at ≤ 600 nm for **1** and **2** is due to light scattering.

surprising that the first singlet transition band of **2** is blue-shifted by as much as approximately 200 nm relative to that of **3**. Note that complex **2** is derived from **3** by replacing one of the pyridine ligands with a CO ligand. The resulting spectral properties can be rationalized, in part, by the strong π -accepting property of CO in **2**, which results in the stabilization of d_π electrons and hence in an increase in the MLCT energy gap.^[16] More details are given in the following sections. On the other hand, although the π -accepting strength of the metal fragment in **1** might be expected to be greater than in **2** because of dual CO coordination by each metal center, the delocalization of the d_π electrons in the diosmium structure offsets the π -accepting effect, so that its first singlet transition energy gap lies between the values of the corresponding energy gaps of **2** and **3**.

Table 5 lists the photophysical data for the complexes **1–3** studied. Complex **2** exhibited an emission maximum at 655 nm in degassed acetonitrile at room temperature. The emission yield and lifetime were determined to be 1.7×10^{-3} and 13.4 ns, respectively. Accordingly, the radiative lifetime was deduced to be approximately 7.9 μ s. The long radiative lifetime and wide separation between the wavelengths at which the peaks for $S_0 \rightarrow S_1$ absorption (515 nm) and emission (655 nm) occur led us to conclude that the emission originates from $T_1 \rightarrow S_0$ phosphorescence. Both phosphorescence intensity and relaxation dynamics are relatively solvent-independent, as supported by the emission at 650 nm in CH_2Cl_2 with an emission yield and observed lifetime of

1.5×10^{-3} and 15.7 ns, respectively. In another approach, attempts to observe luminescence of complexes **1** and **3** throughout the 500–1200-nm region at room temperature unfortunately failed. Instead, as shown in Figure 4, the emission was resolved in an acetonitrile matrix at 77 K. In the case of complex **3**, the emission was observed in the near-IR region with a peak wavelength as long as 935 nm. The emission yield and observed lifetime were measured to be 0.14 and 597 ns, which give a radiative lifetime of 4.3 μ s. Thus, the assignment of this effect as phosphorescence is unambiguous.^[17]

If one considers that both complexes **2** and **3** contain the same chelating 6-pyrazol-3-yl 2,2'-bipyridine ligand, it is intriguing that a slight tuning of complex **2** by removing one carbonyl ligand to form complex **3** results in a drastic bathochromic shift from the red (655 nm) to the near-IR region (935 nm, in CH_3CN). As mentioned earlier, such coarse tuning may be rationalized, in part, by the strong π -accepting property of CO in **2**, which results in the stabilization of d_π electrons and hence in an increase in the $^3\text{MLCT}$ energy gap. Therefore, for complex **2** the contribution of $^3\text{MLCT}$ to the phosphorescence should be drastically reduced. However, according to the spectroscopic observations, the contribution of MLCT to the T_1 state does not seem to be reduced significantly. As shown in Figure 4, for complex **2** the 0–0 onset (≈ 600 nm) of the $S_0 \rightarrow S_1$ absorption nearly overlaps with that of the phosphorescence; therefore, the $^3\text{MLCT}$ contribution must be appreciable. Large MLCT character in the T_1 state implies more contribution of the d_π -electron densities and hence stronger mixing between singlet and triplet manifolds owing to the enhanced spin–orbit coupling. The result is a smaller energy gap between S_1 and T_1 .^[18]

Further insight into the photophysical properties of these complexes can be gained from a theoretical approach (TD-B3LYP//B3LYP/6-31G*; see Experimental Section). Figures 5 and 6 describe the lower-lying transitions. The associated energy gaps in both the singlet and triplet manifolds for complexes **2** and **3** are shown, as well as features of the corresponding occupied and unoccupied frontier orbitals mainly involved in the lower-lying transitions. For both complexes **2** and **3**, the lowest triplet state (T_1) is mainly involved in a HOMO \rightarrow LUMO transition. Except for a slight contribution ($< 10\%$) from CO in **2**, the electron densities of the HOMO are located on the pyrazolate fragment of the chelating tridentate ligand and the central metal atom, whereas those of the LUMO are primarily distributed over the entire bipyridine moiety of the same tridentate ligand. The results clearly indicate that the lowest electronic $S_0 \rightarrow T_1$ transition is dominated by MLCT in combination with a $\pi \rightarrow \pi^*$ transition (ILCT; pyrazolate site (π) \rightarrow bipyridine site (π^*)). Moreover, as shown in Figures 5 and 6, detailed analyses of electron-orbital character clearly indicate that complexes **2** and **3** contain a nearly equal ($\approx 40\%$) contribution of MLCT in the T_1 state. The results for **3** (Figure 6) also indicate that the electron densities of the HOMO and LUMO are equally distributed over the pyrazolate and bipyridine moieties, respectively, of the two tridentate ligands. In sharp

Table 5. Photophysical properties of complexes **1–3** in acetonitrile.

	UV/Vis λ_{max} [nm] ($\epsilon \times 10^{-3}$ [$\text{M}^{-1} \text{cm}^{-1}$])	PL ^[a] λ_{max} [nm]	Q.Y. ^[b]	τ_{obs} [ns]	τ_r [μ s]
1	325(19.2), 470(2.6), 525(1.0) ^[c]	690 ^[d]	0.041 ^[d]	210 ^[d]	5.1
2	385(17.1), 515(1.1)	655 ^[e]	0.0017 ^[e]	13.4 ^[e]	7.9
3	465(9.9), 650(2.8), 715(2.9)	935 ^[d]	0.14 ^[d]	597 ^[d]	4.3

[a] PL = photoluminescence. [b] Q.Y. = quantum yield. [c] Appearance of a shoulder. [d] The emission was detected at 77 K in a frozen matrix. [e] The emission was detected at room temperature in solution.

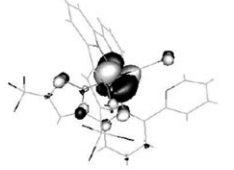

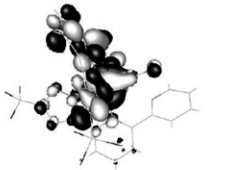
State	Excitation	E_{cal}/eV	$\lambda_{\text{cal}}/\text{nm}$	f	Character
S_1	HOMO \rightarrow LUMO (+74%) HOMO-1 \rightarrow LUMO (+21%)	2.15	575.8	0.0066	MLCT (44.8%)
T_1	HOMO \rightarrow LUMO (+99%)	2.02	613.0	~ 0	MLCT (40.3%)
HOMO-1		HOMO		LUMO	
					

Figure 5. Selected lower-lying transitions and corresponding frontier orbitals for complex **2**.


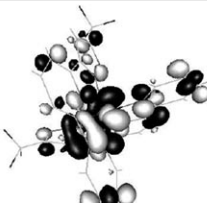
State	Excitation	E_{cal}/eV	$\lambda_{\text{cal}}/\text{nm}$	f	Character
S_1	HOMO \rightarrow LUMO (+90%)	1.67	741.4	0.0122	MLCT (36.7%)
T_1	HOMO \rightarrow LUMO (+100%)	1.44	861.6	~ 0	MLCT (40.8%)
HOMO		LUMO			
					

Figure 6. Selected lower-lying transitions and corresponding frontier orbitals for complex **3**.



State	Excitation	E_{cal}/eV	$\lambda_{\text{cal}}/\text{nm}$	f	Character
S_1	HOMO \rightarrow LUMO (+95%)	2.04	608.8	0.0186	MLCT (60.1%)
T_1	HOMO \rightarrow LUMO (+100%)	1.94	638.8	~ 0	MLCT (63.2%)
HOMO		LUMO			
					

Figure 7. Selected lower-lying transitions and corresponding frontier orbitals for complex **1**.

contrast, in the case of complex **2**, although both pyrazolate sites do contribute to the HOMO, the bipyridine moiety that contains a dangling, nonbonded pyridyl group is no longer involved in the LUMO. The results indicate a significant decrease in the π conjugation; that is, a decrease in the energy of the π orbitals and an increase in the energy of the π^* orbitals, and hence an increase in the π - π^* energy gap. This result, in combination with the decrease in the energy of the d_{π} orbital due to the π -accepting effect of CO, rationalizes the significant increase in the S_0 - T_1 energy gap in **2**.

In view of the relaxation dynamics of complexes **1**-**3**, the corresponding phosphorescence is in the region that extends from deep red to near IR. Thus, the rather weak emission properties can be rationalized qualitatively by using an empirical energy-gap law.^[19] Upon a decrease in the energy gap, rapid quenching may take place by $T_1 \rightarrow S_0$ intersystem crossing through the coupling of certain high-frequency vibration motions or those vibration motions with a high density of states, and subsequent collisional deactivation by the solvent in a fluid solution. In the case of complex **3**, which

The calculated wavelengths of $S_0 \rightarrow T_1$ transition of 613 and 862 nm are in good qualitative agreement with the 0-0 onset of phosphorescence located at approximately 580 and 800 nm, respectively, in acetonitrile. The deviation of the results of this theoretical approach from the experimental results may be explained plausibly by the negligence of solvation effects in the gas-phase ab initio approach. Clearly, the theoretical level adopted in this study is suitable for studying the photophysical properties of these complexes in a qualitative manner.

In the case of complex **1**, the wavelength at which the phosphorescence peak occurs was resolved to be 690 nm in an acetonitrile matrix at 77 K. Apparently, the emission energy gap is between that of **2** and **3**. As mentioned before, although the π -accepting strength in **1** should be stronger as a result of the dual CO coordination of each Os atom, the delocalization of the d_{π} electrons in the diosmium structure may offset the π -accepting effect. This viewpoint is also supported by the theoretical approach, the results of which indicate that the transition is split equally between the two Os d_{π} electrons and the pyrazolate π electrons, and between the π^* orbitals of the two bipyridine moieties (Figure 7). The $S_0 \rightarrow T_1$ transition was calculated to occur at 638 nm; this value lies between the corresponding transition wavelengths calculated for complexes **2** and **3**, as expected.

has an energy gap as low as approximately 10700 cm^{-1} ($\approx 935\text{ nm}$), apparently rapid quenching occurs, and this phenomenon explains the lack of emission at room temperature. However, the emission peak at 690 nm (77 K) of **1** is not much lower in energy than the weak phosphorescence at 655 nm observed for **2**. Accordingly, the non-emissive properties of **1** at room temperature are intriguing. In our opinion, the results may be rationalized plausibly by correlating the rapid radiationless deactivation with the increase in vibrational modes that are channeled into the radiationless deactivation pathways. From a comparison of the data listed in Figures 5 and 7, it is clear that despite a simple contribution, that is, a HOMO \rightarrow LUMO transition to the T_1 state, **1** displays much broader spreading of the electron density than **2** in both the HOMO and the LUMO. The results can be rationalized tentatively by considering that the two tridentate ligands in **1** are subject to identical coordinating environments. This feature of the structure of **1**, in combination with the framework constructed by the relatively weak Os–Os bond, increases statistically the amount of nuclear motions that could induce the quenching of emission.

We performed a temperature-dependent study on complex **3** to determine the effect of thermal activation on the nonradiative deactivation. Because of the lack of emission by **3** at ambient temperature, the experiment was performed in the temperature range $255\text{--}190\text{ K}$. The plot of the logarithm of $(k_{\text{obs}} - k_r)$ versus $1/T$, in which k_{obs} and k_r are the observed and radiative decay rate constants, gave a sufficiently straight line, from which a ΔE_a value of 0.5 kcal mol^{-1} and a pre-exponential factor of $4.5 \times 10^7\text{ s}^{-1}$ were deduced (Figure 8). The results indicate that the nonradiative decay rate may be dominated by motions of rather low frequencies. These motions possibly involve geometry-distortion motions coupled with $T_1 \rightarrow S_0$ intersystem crossing. Although specific modes that induce radiationless transition are pending resolution at this stage, such a small energy gap should lead statistically to an increase in active vibration modes involved in the radiationless deactivation.

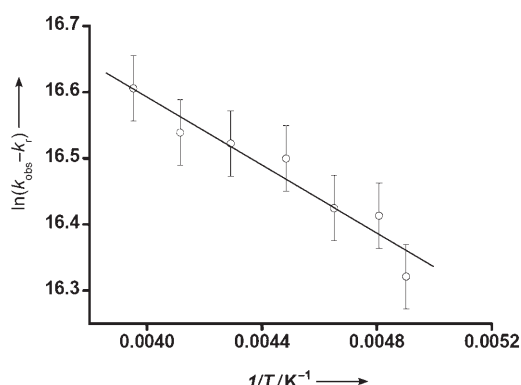


Figure 8. The Arrhenius plot of $\ln(k_{\text{obs}} - k_r)$ versus $1/T$ ($T = 255\text{--}190\text{ K}$) of complex **3** in MeOH, in which k_{obs} denotes the observed decay rate constant and k_r is the radiative decay rate constant calculated at 77 K (see Table 5; it is assumed that k_r is independent of the solvent used).

Conclusions

In summary, we have prepared and characterized a series of osmium complexes **1–3** with the tridentate chelating ligand (fpbpy)H. Upon the transformation of **2** into **3** by elimination of CO, an extremely large change in the wavelength at which phosphorescence occurs (from 655 to 935 nm) was observed. The results were rationalized qualitatively by the strong π -accepting character of CO, which lowers the energy of the Os d_π orbital and leads to an increase in the MLCT energy gap, in combination with a decrease in π -electron conjugation as a result of the dangling pyridyl group in **2**. Further support for this rationale was provided by the time-dependent DFT approach, which revealed that the $S_0 \rightarrow T_1$ transition for both **2** and **3** mainly involves osmium-to-bipyridine $^3\pi-\pi^*$ intraligand charge transfer. The relatively weak near-infrared emission can be rationalized tentatively by the energy-gap law, according to which the radiationless deactivation may be governed by certain low-frequency motions with a high density of states. One current focus of research on OLEDs has been Os^{II}- and Ru^{II}-based phosphorescence emitters;^[20] complex **3**, which emits in the near-IR region, and/or relevant derivatives may find application in the fabrication of photovoltaic devices,^[21] near-IR emitters, and even OLEDs.^[22] Research focused on these objectives is in progress.

Experimental Section

General Information and Materials

All reactions were performed under a nitrogen atmosphere in anhydrous solvents or solvents treated with an appropriate drying reagent. Mass spectra were recorded on a JEOL SX-102 A instrument operating in electron-impact (EI) mode or fast-atom-bombardment (FAB) mode. ^1H and ^{19}F NMR spectra were recorded on Varian Mercury-400 or INOVA-500 instruments. Elemental analyses were conducted at the NSC Regional Instrumentation Center at National Chiao Tung University.

Syntheses

1: A mixture of $[\text{Os}_3(\text{CO})_{12}]$ (160 mg , 0.18 mmol) and (fpbpy)H (150 mg , 0.52 mmol) in anhydrous DGME (50 mL) was heated at 170°C for 24 h . After the reaction mixture had cooled to room temperature, the solvent was removed under vacuum, and the residue was purified by column chromatography on silica gel (ethyl acetate/acetone = $9:1$). $[\text{Os}_2(\text{CO})_4(\text{fpbpy})]$ (**1**; 105 mg , 0.10 mmol , 38%) was obtained as a red crystalline solid by recrystallization from dimethyl sulfoxide (DMSO) and diethyl ether at room temperature. IR (CH_2Cl_2): $\tilde{\nu} = 2010\text{ (s)}$, 1961 (m) , 1926 (s) , $1908\text{ cm}^{-1}\text{ (m, sh; C=O)}$; $^1\text{H NMR}$ (400 MHz , $[\text{D}_6]\text{acetone}$, 298 K , tetramethylsilane (TMS)): $\delta = 9.30\text{ (dd, } J_{\text{H,H}} = 6.0, 1.0\text{ Hz, 1H)}$, $8.18\text{ (dd, } J_{\text{H,H}} = 8.0, 2.0\text{ Hz, 2H)}$, $8.09\text{ (td, } J_{\text{H,H}} = 8.0, 2.0\text{ Hz, 1H)}$, $7.92\text{ (t, } J_{\text{H,H}} = 8.0\text{ Hz, 1H)}$, $7.68\text{ (td, } J_{\text{H,H}} = 6.0, 2.0\text{ Hz, 1H)}$, $7.18\text{ (dd, } J_{\text{H,H}} = 6.0, 1.0\text{ Hz, 1H)}$, 6.36 ppm (s, 1H) ; MS (FAB, ^{192}Os): m/z (%) calcd for $\text{C}_{32}\text{H}_{16}\text{F}_6\text{N}_8\text{O}_4\text{Os}_2$: 1074.04 (100) $[M]^+$; found: 1073.00 ; elemental analysis: calcd (%) for $\text{C}_{32}\text{H}_{16}\text{F}_6\text{N}_8\text{O}_4\text{Os}_2 + \text{DMSO} + \text{C}_4\text{H}_{10}\text{O}$: C 37.31 , N 9.16 , H 2.64 ; found: C 36.56 , N 9.79 , H 2.31 .

2 (Method A): A mixture of $[\text{Os}_3(\text{CO})_{12}]$ (150 mg , 0.17 mmol) and (fpbpy)H (290 mg , 1.0 mmol) in anhydrous DGME (50 mL) was heated at 180°C for 24 h . After the reaction mixture had cooled to room temperature, the solvent was removed under vacuum, and the residue was purified by column chromatography on silica gel (ethyl acetate/acetone =

9:1). [Os(CO)(fpbpy)₂] (**2**; 72 mg, 0.09 mmol, 55%) was obtained as a deep-red crystalline solid by recrystallization from acetone and diethyl ether at room temperature. IR (CH₂Cl₂): $\tilde{\nu}$ = 1973 cm⁻¹ (C=O); ¹H NMR (400 MHz, [D₆]acetone, 298 K, TMS): δ = 8.65 (dd, *J*_{H,H} = 5.0, 1.0 Hz, 1H), 8.51 (d, *J*_{H,H} = 8.0 Hz, 1H), 8.40 (d, *J*_{H,H} = 8.0 Hz, 1H), 8.35 (d, *J*_{H,H} = 8.0 Hz, 1H), 8.21 (dd, *J*_{H,H} = 8.0, 1.0 Hz, 1H), 8.15–8.05 (m, 4H), 7.92 (d, *J*_{H,H} = 6.0 Hz, 1H), 7.79 (td, *J*_{H,H} = 8.0, 2.0 Hz, 1H), 7.60 (dd, *J*_{H,H} = 8.0, 2.0 Hz, 1H), 7.48 (t, *J*_{H,H} = 6.0 Hz, 1H), 7.44 (td, *J*_{H,H} = 5.0, 1.0 Hz, 1H), 7.27 (s, 1H), 7.18 ppm (s, 1H); MS (FAB, ¹⁹²Os): *m/z* (%) calcd for C₂₉H₁₆F₆N₈OOs: 798.10 (100) [*M*]⁺; found 797.00; elemental analysis: calcd (%) for C₂₉H₁₆F₆N₈OOs: C 43.72, N 14.06, H 2.02; found: C 43.79, N 13.60, H 2.46.

2 (Method B): A mixture of **1** (50 mg, 0.05 mmol) and (fpbpy)H (30 mg, 0.1 mmol) in DGME (20 mL) was heated at 170 °C for 24 h. After the reaction mixture had cooled to room temperature, the solvent was removed under vacuum, and the residue was purified by column chromatography on silica gel (ethyl acetate/acetone = 9:1) to give a mixture of **1** (32 mg, 0.03 mmol, 60%), **2** (4 mg, 0.005 mmol, 6%), and **3** (5 mg, 0.006 mmol, 7%).

3: A mixture of **2** (50 mg, 0.06 mmol) and anhydrous Me₃NO (50 mg, 0.66 mmol) in anhydrous DGME (30 mL) was heated at 180 °C for 24 h. After the reaction mixture had cooled to room temperature, the solvent was removed under vacuum, and the residue was purified by column chromatography on silica gel (ethyl acetate/acetone = 9:1) to give a mixture of **2** (25 mg, 0.03 mmol, 50%) and [Os(fpbpy)₂] (**3**; 15 mg, 0.02 mmol, 32%). Black crystals of **3** were obtained by recrystallization from a mixture of methanol and diethyl ether at room temperature. ¹H NMR (400 MHz, [D₆]acetone, 298 K, TMS): δ = 8.35 (d, *J*_{H,H} = 8.0 Hz, 1H), 8.30 (d, *J*_{H,H} = 8.0 Hz, 1H), 8.09 (d, *J*_{H,H} = 8.0 Hz, 1H), 7.50 (t, *J*_{H,H} = 8.0 Hz, 1H), 7.43 (td, *J*_{H,H} = 8.0, 2.0 Hz, 1H), 7.04 (d, *J*_{H,H} = 5.6 Hz, 1H), 6.95 (s, 1H), 6.88 ppm (td, *J*_{H,H} = 6.0, 2.0 Hz, 1H); MS (FAB, ¹⁹²Os): *m/z* (%) calcd for C₂₈H₁₆F₆N₈O₂Os: 770.10 (100) [*M*]⁺; found: 770.00; elemental analysis: calcd (%) for C₂₈H₂₀OF₆N₈O₂Os: C 43.50, N 13.99, H 2.52; found: C 43.40, N 13.93, H 2.56.

X-ray Diffraction Studies

Single-crystal X-ray diffraction data were collected on a Bruker SMART Apex CCD diffractometer by using MoK α radiation (λ = 0.71073 Å) and the SMART program. Cell refinement and data reduction were performed with the SAINT program. The structure was determined by using the SHELXTL/PC program and refined by using full-matrix least squares. It was observed that single crystals of **1** contain two DMSO molecules in the unit cell, and single crystals of **3** contain 3.5 molecules of methanol and one water of hydration in the unit cell. The crystallographic refinement parameters of complexes **1**, **2**, and **3** are summarized in Table 1. CCDC-619115 (**1**), -619116 (**2**), and -619117 (**3**) contain the supplementary crystallographic data (excluding structure factors) for this paper. These data can be obtained free of charge from the Cambridge Crystallographic Data Centre at www.ccdc.cam.ac.uk/data_request/cif.

Spectral Measurement

Steady-state absorption and emission spectra were recorded with a Hitachi (U-3310) spectrophotometer and an Edinburgh (FS920) fluorimeter, respectively. For measuring the near-infrared (NIR) emission, a continuous-wave Ar-ion laser (514 nm, Coherent Innova 90) was used as the excitation source and was modulated at approximately 140 Hz by a mechanical chopper. The NIR phosphorescence was then recorded at a direction perpendicular to the pump beam and sent through a lock-in amplifier (Stanford Research System SR830) before being detected by an NIR-sensitive photomultiplier tube (Hamamatsu R5509-72) operated at -80 °C. To measure the emission quantum yield of **1** and **3**, the fluorescence dye IR125 (Exciton, Dayton, Ohio) with a known emission yield of $\Phi \approx 0.11$ ($\lambda_{\text{max}} \approx 930$ nm)^[23] in DMSO served as a standard. CH₂Cl₂ ($\Phi \approx 0.44$, $\lambda_{\text{max}} \approx 650$ nm)^[24] was used as a standard for estimating the quantum yield of **2**. Typical-lifetime studies were performed with an Edinburgh FL 1900 photon-counting system with a hydrogen-filled or nitrogen lamp as the excitation source. Data were analyzed by using the nonlinear least-squares procedure in combination with an iterative convolution

method. The emission decays were analyzed by the sum of exponential functions, which allows partial removal of the instrument time broadening and provides a temporal resolution of approximately 200 ps. For the phosphorescence-lifetime measurements in the μ s region, the second harmonic of an Nd:YAG laser (532 nm, 8 ns, Continuum Surelite II) was used as the excitation source. Emission decay was then detected by a photomultiplier tube and averaged over 512 shots by using an oscilloscope (model TDS 3012, Tektronix).

Computational Methodology

Time-dependent B3LYP calculations were based on the geometry-optimized structures at the B3LYP level. The basis set used for both geometry optimization and the calculation of the excitation energy was a double- ζ -quality basis set consisting of the effective core potentials (LANL2DZ) for osmium atoms described by Hay and Wadt,^[25] a 6-31G* basis set was employed for the H, C, N, F, and O atoms. A relativistic effective core potential (ECP) replaced the inner-core electrons of Os to leave the outer-core (5s²5p⁶) electrons and the 5d⁶6s² valence electrons. Typically, the lowest triplet and singlet roots of the nonhermitian eigenvalue equations were obtained to determine the vertical excitation energies. Oscillator strengths were deduced from the dipole transition matrix elements (for singlet states only). The excited-state time-dependent DFT calculations were carried out by using Gaussian03 in a manner similar to that mentioned in our previous publications.^[26]

Acknowledgements

The authors are grateful for financial support from the National Science Council, the Ministry of Economy, and the National Center of High-Performance Computing.

- [1] a) P. J. Steel, *Acc. Chem. Res.* **2005**, *38*, 243; b) G. Chelucci, R. P. Thummel, *Chem. Rev.* **2002**, *102*, 3129; c) R. Ziessel, *Coord. Chem. Rev.* **2001**, *216–217*, 195; d) U. S. Schubert, C. Eschbaumer, *Angew. Chem.* **2002**, *114*, 3016; *Angew. Chem. Int. Ed.* **2002**, *41*, 2892.
- [2] a) K. P. Balashev, M. V. Puzyk, V. S. Kotlyar, M. V. Kulikova, *Coord. Chem. Rev.* **1997**, *159*, 109; b) B. Ma, P. I. Djurovich, M. E. Thompson, *Coord. Chem. Rev.* **2005**, *249*, 1501.
- [3] a) P.-C. Wu, J.-K. Yu, Y.-H. Song, Y. Chi, P.-T. Chou, S.-M. Peng, G.-H. Lee, *Organometallics* **2003**, *22*, 4938; b) J.-K. Yu, Y.-H. Hu, Y.-M. Cheng, P.-T. Chou, S.-M. Peng, G.-H. Lee, A. J. Carty, Y.-L. Tung, S.-W. Lee, Y. Chi, C.-S. Liu, *Chem. Eur. J.* **2004**, *10*, 6255; c) P. Coppo, E. A. Plummer, L. De Cola, *Chem. Commun.* **2004**, 1774; d) C.-H. Yang, S.-W. Li, Y. Chi, Y.-M. Cheng, Y.-S. Yeh, P.-T. Chou, G.-H. Lee, C.-H. Wang, C.-F. Shu, *Inorg. Chem.* **2005**, *44*, 7770.
- [4] a) S. Welter, N. Salluce, P. Belser, M. Groeneveld, L. De Cola, *Coord. Chem. Rev.* **2005**, *249*, 1360; b) A. Beyeler, P. Belser, *Coord. Chem. Rev.* **2002**, *230*, 29; c) M. G. Colombo, A. Hauser, H. U. Gudel, *Top. Curr. Chem.* **1994**, *171*, 143.
- [5] a) M. K. Nazeeruddin, C. Klein, P. Liska, M. Graetzel, *Coord. Chem. Rev.* **2005**, *249*, 1460; b) H. Yersin, *Top. Curr. Chem.* **2004**, *241*, 1; c) P.-T. Chou, Y. Chi, *Chem. Eur. J.* **2006**, DOI: 10.1002/chem.200601272.
- [6] a) P. Steenwinkel, R. A. Gossage, G. Van Koten, *Chem. Eur. J.* **1998**, *4*, 759; b) M. E. van der Boom, D. Milstein, *Chem. Rev.* **2003**, *103*, 1759; c) I. Omae, *Coord. Chem. Rev.* **2004**, *248*, 995.
- [7] a) R. Hage, J. G. Haasnoot, J. Reedijk, R. Wang, J. G. Vos, *Inorg. Chem.* **1991**, *30*, 3263; b) R. Hage, J. G. Haasnoot, J. Reedijk, J. G. Vos, *Chemtracts: Inorg. Chem.* **1992**, *4*, 75; c) F.-C. Hsu, Y.-L. Tung, Y. Chi, C.-C. Hsu, Y.-M. Cheng, M.-L. Ho, P.-T. Chou, S.-M. Peng, A. J. Carty, *Inorg. Chem.* **2006**, *45*, 10188.
- [8] a) E. Baranoff, J.-P. Collin, L. Flamigni, J.-P. Sauvage, *Chem. Soc. Rev.* **2004**, *33*, 147; b) E. A. Medlycott, G. S. Hanan, *Chem. Soc. Rev.* **2005**, *34*, 133; c) D. R. McMillin, J. J. Moore, *Coord. Chem. Rev.* **2002**, *229*, 113; d) D. K. Crites Tears, D. R. McMillin, *Coord. Chem. Rev.* **2001**, *211*, 195; e) A. J. Wilkinson, A. E. Goeta, C. E. Foster,

- J. A. G. Williams, *Inorg. Chem.* **2004**, *43*, 6513; f) P. R. Andres, U. S. Schubert, *Adv. Mater.* **2004**, *16*, 1043.
- [9] a) M. A. Halcrow, *Coord. Chem. Rev.* **2005**, *249*, 2880; b) R. Mukherjee, *Coord. Chem. Rev.* **2000**, *203*, 151; c) T. Yutaka, S. Obara, S. Ogawa, K. Nozaki, N. Ikeda, T. Ohno, Y. Ishii, K. Sakai, M. Haga, *Inorg. Chem.* **2005**, *44*, 4737.
- [10] K. L. V. Mann, E. Psillakis, J. C. Jeffery, L. H. Rees, N. M. Harden, J. A. McCleverty, M. D. Ward, D. Gatteschi, F. Totti, F. E. Mabbs, E. J. L. McInnes, P. C. Riedi, G. M. Smith, *J. Chem. Soc. Dalton Trans.* **1999**, 339.
- [11] a) E. Psillakis, J. C. Jeffery, J. A. McCleverty, M. D. Ward, *Chem. Commun.* **1997**, 479; b) J. S. Fleming, E. Psillakis, S. M. Couchman, J. C. Jeffery, J. A. McCleverty, M. D. Ward, *J. Chem. Soc. Dalton Trans.* **1998**, 537.
- [12] P.-T. Chou, Y. Chi, *Eur. J. Inorg. Chem.* **2006**, 3319.
- [13] E. C. Constable, F. Heitzler, M. Neuburger, M. Zehnder, *J. Am. Chem. Soc.* **1997**, *119*, 5606.
- [14] a) W.-S. Yu, C.-C. Cheng, Y.-M. Cheng, P.-C. Wu, Y.-H. Song, Y. Chi, P.-T. Chou, *J. Am. Chem. Soc.* **2003**, *125*, 10800; b) C.-C. Cheng, W.-S. Yu, P.-T. Chou, S.-M. Peng, G.-H. Lee, P.-C. Wu, Y.-H. Song, Y. Chi, *Chem. Commun.* **2003**, 2628.
- [15] C. C. Cheng, J. G. Goll, G. A. Neyhart, T. W. Welch, P. Singh, H. H. Thorp, *J. Am. Chem. Soc.* **1995**, *117*, 2970.
- [16] a) Y.-L. Chen, S.-W. Lee, Y. Chi, K.-C. Hwang, S. B. Kumar, Y.-H. Hu, Y.-M. Cheng, P.-T. Chou, S.-M. Peng, G.-H. Lee, S.-J. Yeh, C.-T. Chen, *Inorg. Chem.* **2005**, *44*, 4287; b) Y.-M. Cheng, Y.-S. Yeh, M.-L. Ho, P.-T. Chou, P.-S. Chen, Y. Chi, *Inorg. Chem.* **2005**, *44*, 4594.
- [17] H.-Y. Chen, C.-H. Yang, Y. Chi, Y.-M. Cheng, Y.-S. Yeh, P.-T. Chou, H.-Y. Hsieh, C.-S. Liu, S.-M. Peng, G.-H. Lee, *Can. J. Chem.* **2006**, *84*, 309.
- [18] a) J. Li, P. I. Djurovich, B. D. Alleyne, M. Yousufuddin, N. N. Ho, J. C. Thomas, J. C. Peters, R. Bau, M. E. Thompson, *Inorg. Chem.* **2005**, *44*, 1713; b) J. Kavitha, S.-Y. Chang, Y. Chi, J.-K. Yu, Y.-H. Hu, P.-T. Chou, S.-M. Peng, G.-H. Lee, Y.-T. Tao, C.-H. Chien, A. J. Carty, *Adv. Funct. Mater.* **2005**, *15*, 223.
- [19] a) E. M. Kober, J. V. Caspar, R. S. Lumpkin, T. J. Meyer, *J. Phys. Chem.* **1986**, *90*, 3722; b) P. T. A. Perkins, D. B. Pourreau, T. L. Netzel, K. S. Schanze, *J. Phys. Chem.* **1989**, *93*, 4511.
- [20] a) Y.-L. Tung, L.-S. Chen, Y. Chi, P.-T. Chou, Y.-M. Cheng, E. Y. Li, G.-H. Lee, C.-F. Shu, F.-I. Wu, A. J. Carty, *Adv. Funct. Mater.* **2006**, *16*, 1615; b) Y.-L. Tung, S.-W. Lee, Y. Chi, Y.-T. Tao, C.-H. Chien, Y.-M. Cheng, P.-T. Chou, S.-M. Peng, C.-S. Liu, *J. Mater. Chem.* **2005**, *15*, 460; c) Y.-H. Niu, Y.-L. Tung, Y. Chi, C.-F. Shu, J. H. Kim, B. Chen, J. Luo, A. J. Carty, A. K.-Y. Jen, *Chem. Mater.* **2005**, *17*, 3532; d) Y.-L. Tung, P.-C. Wu, C.-S. Liu, Y. Chi, J.-K. Yu, Y.-H. Hu, P.-T. Chou, S.-M. Peng, G.-H. Lee, Y. Tao, A. J. Carty, C.-F. Shu, F.-I. Wu, *Organometallics* **2004**, *23*, 3745.
- [21] a) N. Robertson, *Angew. Chem.* **2006**, *118*, 2398; *Angew. Chem. Int. Ed.* **2006**, *45*, 2338; b) M. Graetzel, *Inorg. Chem.* **2005**, *44*, 6841.
- [22] a) S. D. Bergman, D. Gut, M. Kol, C. Sabatini, A. Barbieri, F. Barigelletti, *Inorg. Chem.* **2005**, *44*, 7943; b) C.-Y. Wong, G. S. M. Tong, C.-M. Che, N. Zhu, *Angew. Chem.* **2006**, *118*, 2760; *Angew. Chem. Int. Ed.* **2006**, *45*, 2694; c) M. I. J. Polson, F. Loiseau, S. Campagna, G. S. Hanan, *Chem. Commun.* **2006**, 1301; d) T. Del Cano, K. Hashimoto, H. Kageyama, J. A. De Saja, R. Aroca, Y. Ohmori, Y. Shirota, *Appl. Phys. Lett.* **2006**, *88*, 071117.
- [23] R. C. Benson, H. A. Jues, *J. Chem. Eng. Data* **1977**, *22*, 379.
- [24] J. M. Drake, M. L. Lesiecki, D. M. Camaioni, *Chem. Phys. Lett.* **1985**, *113*, 530.
- [25] a) P. J. Hay, W. R. Wadt, *J. Chem. Phys.* **1985**, *82*, 270; b) W. R. Wadt, P. J. Hay, *J. Chem. Phys.* **1985**, *82*, 284; c) P. J. Hay, W. R. Wadt, *J. Chem. Phys.* **1985**, *82*, 299.
- [26] a) S.-W. Li, Y.-M. Cheng, Y.-S. Yeh, C.-C. Hsu, P.-T. Chou, S.-M. Peng, G.-H. Lee, Y.-L. Tung, P.-C. Wu, Y. Chi, F.-I. Wu, C.-F. Shu, *Chem. Eur. J.* **2005**, *11*, 6347; b) Y.-L. Chen, S.-W. Li, Y. Chi, Y.-M. Cheng, S.-C. Pu, Y.-S. Yeh, P.-T. Chou, *ChemPhysChem* **2005**, *6*, 2012; c) J.-K. Yu, Y.-M. Cheng, Y.-H. Hu, P.-T. Chou, Y.-L. Chen, S.-W. Lee, Y. Chi, *J. Phys. Chem. B* **2004**, *108*, 19908; d) Y.-S. Yeh, Y.-M. Cheng, P.-T. Chou, G.-H. Lee, C.-H. Yang, Y. Chi, C.-F. Shu, C.-H. Wang, *ChemPhysChem* **2006**, *7*, 2294.

Received: August 28, 2006

Published online: December 14, 2006